Research Paper

# Interfacial charge transfer in oxygen deficient TiO$_2$-graphene quantum dot hybrid and its influence on the enhanced visible light photocatalysis

Gone Rajender[a], Jitendra Kumar[b], P.K. Giri[a,b,*]

[a] Department of Physics, Indian Institute of Technology Guwahati, Guwahati 781039, India
[b] Centre for Nanotechnology, Indian Institute of Technology Guwahati, Guwahati 781039, India

## ARTICLE INFO

## ABSTRACT

The present work focuses on understanding the heterojunction formation of graphene quantum dots (GQDs) and oxygen deficient TiO$_2$ nanoparticle hybrid system and its enhanced photocatalytic activity under visible light illumination. We explain the formation of TiO$_2$-GQD heterojunction through the bonding between oxygen vacancy sites in TiO$_2$ and in-plane oxygen functional (epoxy) groups in GQDs possibly via C−O−Ti bonds. Our FTIR, XPS and Raman results lend support to the proposed mechanism of heterojunction formation. In the TiO$_2$/GQD hybrid, the Raman E$_g$(1) peak of anatase TiO$_2$ is blue shifted indicating the strong interaction between the GQD and TiO$_2$. The heterojunction formation was simulated through the density functional theory (DFT) calculation to obtain the optical spectrum on the hybrid between oxygen deficient TiO$_2$ and oxygen functionalized GQDs. Interestingly, the calculated results for the hybrid structure show strong optical absorption in the visible to near infrared region, which is in close agreement with the experimental results. The TiO$_2$-GQD heterojunction exhibits enhanced photocatalytic degradation (97%) of MB due to the facile interfacial charge separation, as revealed from the steady state and time resolved photoluminescence studies. Interestingly, the photoluminescence intensity of the TiO$_2$-GQD heterojunction was partially quenched indicating the electron transfer from GQDs to TiO$_2$. The degradation rate constant (first order) for TiO$_2$-GQD hybrid is 5.2 times higher than that of the TiO$_2$. Free radical scavenger test revealed that ·OH radical played a major role in MB degradation as compared to O$_2^{\cdot-}$ radical. These results are significant for the development of metal free catalysts based on carbon nano-materials for ensuing optoelectronic, energy and environmental applications.

## 1. Introduction

Titanium dioxide (TiO$_2$) is one of the promising materials for various applications ranging from water splitting, solar cells, energy storage device, optoelectronic devices, photocatalysis etc. [1–8]. Among different polymorphs of TiO$_2$, anatase phase is most preferable for photocatalytic application, due to its highly oxidizing power, high surface area, ability to generate more free radicals and charge carrier transport etc. [3–5,9]. Despite its good performance and stability, TiO$_2$ based photocatalysts have limited applications because of its wide band gap energy (anatase 3.2 eV), which impede the efficient utilization of visible light and as a consequence yields low photocatalytic efficiency using solar light driven photocatalysis, since solar spectrum consists of only 3–5% of UV and 44% of visible light. On other hand, the high recombination rate of photo generated charge carries is another cause of concern for the low photocatalysis efficiency [10]. Band gap narrowing and efficient charge separation can promote a high rate of photocatalytic degradation for various synthetic dyes and pigments that

are produced in large scale at industry. Notably, the presence of dye effluents cannot be discarded, as it greatly affects the environmental eco system [11,12]. To improve the photocatalytic efficiency, heterogeneous catalysts based on TiO$_2$ and conventional semiconductor quantum dots (QDs), such as CdS, CdSe, PbS, etc. have been proposed [6,13–15]. To achieve the facile electron and hole separation, one can engineer the proper heterojunction using QDs and TiO$_2$ nanostructure [6]. Apart from these, semiconductor QDs are known to be highly unstable to hole oxidation when light irradiated in liquid medium [16]. Besides, semiconductor QDs based on Cd certainly causes the environmental problems due to release of highly toxic Cd ions into the solution by the photo oxidation [2,16]. Hence, it is necessary to fabricate heterojunction based on carbon QDs and TiO$_2$ for ensuing applications.

Graphene QDs are emerging class of zero-dimensional (0D) material and it show pronounced quantum confinement, plenty of edge states and functional groups [17–20]. Moreover, simple synthesis procedure, low toxicity, stable photoluminescence (PL), and excellent solubility

properties of GQDs are highly advantageous than the conventional semiconductor QDs. Consequently, GQDs are being explored for studying the fundamental properties as well as their applications in optoelectronic devices, sensors, bioimaging, resistive switching, energy, environmental cleaning, etc. [19,21–26]. It has been proposed that the combination of GQDs and TiO₂ is a model heterojunction for visible light photocatalysis and other emerging applications [27,28]. The envisaged advantage of GQDs over conventional semiconductor QDs is to cross the Shockley–Queisser limit, where the hot charge carriers are the sources in solar to electric energy conversion process [29].

One of the simplest ways for large scale synthesis of GQDs is the ultrasonication method by separation from the carbon based materials [24,26,30,31]. Interestingly, ultrasonication is a green and an inexpensive approach for the introduction of defects in TiO₂ [32–34] and the same has been used for the preparation of composite materials [13–15,34–37]. It has been proposed that during the ultrasonication, ultrasonic waves produce an intense localized hot spot in the solid composite [34,38,39]. Previous reports indicate that TiO₂ nanotubes array and GQDs hybrids are good candidates for UV and visible light photocatalysis [40,41], and GQD-TiO₂ nanowire hybrid for photoelectrochemical (PEC) hydrogen fuel production [42]. Xing et al. studied the graphene and TiO₂ hybrid formation through the OH functional groups [36]. Umrao et al. proposed the C−O−Ti bond formation in TiO₂-graphene system due to the free electron interaction of both the materials [37]. However, the actual pathway that leads to the formation of the TiO₂-GQD hybrid has not been addressed in the literature. GQDs are known to be ultrafine size pieces of graphene materials. Due to the ultrafine size and high ratio of edge to basal plane, carbon atoms in GQDs possess the edge states and edge oxygen functional groups [43–46]. In this regard, GQDs have meagre in-plane oxygen functional groups than that of graphene materials. Thus, we believe that in GQDs mostly the edge oxygen functional groups rearrangement or in-plane epoxy disorder is necessary in order to form the hybrid. To our knowledge, the actual pathway that leads to the formation of the TiO₂-GQD heterojunction in the oxygen deficient TiO₂ and GQDs enriched with in-plane oxygen function groups has not been addressed in the literature. Thus, it is of significant interest to study the formation of TiO₂-GQD heterojunction, the interfacial charge carrier dynamics in the heterojunction and its influence on the visible light photocatalysis.

Herein, we study the formation mechanism of TiO₂-GQD heterojunction and its application in the improved visible light photocatalytic degradation of methylene blue (MB), a model dye. Based on our experimental results of Raman, PL, X-ray photoelectron spectroscopy (XPS), Fourier transform infrared (FTIR) spectroscopy and Thermogravimetric analysis (TGA), we propose ultrasonication induced oxygen vacancy and in-plane epoxy functional group mediated possible C−O−Ti bond formation in TiO₂-GQD hybrid, for the first time. The proposed heterojunction formation is simulated by DFT calculation that shows a close agreement with the experimental results. XPS studies demonstrate that reduction of edge oxygen functional groups in GQDs is due to the hybrid formation with the TiO₂. We probe the change in oxygen vacancy defects in TiO₂ from the PL studies after the decoration of GQDs onto the TiO₂, and these results are corroborated by time resolved (TR) PL, Raman and electron paramagnetic resonance (EPR) studies. FTIR and XPS analyses suggest the possible presence of C−O−Ti bonds in the hybrid system. Finally, we explore the use of the TiO₂-GQD hybrid for the visible light photocatalytic degradation of MB. To understand the different free radicals involved in the photodegradation of MB, we perform the scavenger test and our studies suggest that the ·OH radical plays a major role in the MB degradation. The mechanism of interfacial charge transfer and the possible degradation pathway of MB are discussed. Significance of these results for controlled fabrication of metal free carbon nanomaterial based hybrids catalysts for energy and environmental applications are discussed.

## 2. Experimental details

### 2.1. Fabrication of GQDs and TiO₂ nanoparticle hybrids

Details of the fabrication of GQDs and TiO₂ NPs are provided in the supplementary information (S1). TiO₂ NPs (pristine and ball milled) and GQDs (weight ratio 1:1) are mixed together and dispersed in DI water. Next, the mixture was ultrasonicated (40 kHz) for 1hr and subsequently centrifuged, dried to get the solid powder. Pristine and 16 h ball milled TiO₂ NPs [47] samples are denoted as T0 and T16, respectively. The hybrid samples of T0 and T16 each mixed with GQDs and ultrasonicated are denoted as T0/GQD and T16/GQD, respectively. We also performed the ultrasonication treatment on sample T0 and it is denoted as T0S. One set of hybrid sample is prepared only by mixing and stirring method without any ultrasonication, and the sample is termed as T16/GQDM.

### 2.2. Characterization techniques

Crystallinity and phase of the as-prepared samples are studied by powder X-ray diffraction (XRD) with Rigaku RINT 2500 TTRAX-III, Cu-K$_\alpha$ radiation. The morphological features and crystallinity of the samples are obtained with transmission electron microscopy (TEM), high-resolution (HR) TEM and selected area electron diffraction (SAED) pattern using a JEOL 2100 (Japan) operating at 200 kV. Micro-Raman measurements were performed using a high resolution spectrometer (Horiba, LabRam HR) with an excitation wavelength of 488 nm. Excitation source was focused with 100X objective lens and 1 mW of laser power used to avoid the laser heating and damage to the sample. The Raman signal was collected by a CCD in a back scattering geometry sent through a multimode fibre grating of 1800 grooves per mm. XPS data were obtained with a PHI X-Tool automated photoelectron spectrometer (ULVAC-PHI, Inc.) using Al K$\alpha$ X-ray beam (1486.6 eV) with a beam current of 20 mA. The UV–vis absorption and diffuse reflectance spectroscopy (DRS) measurements were performed using a commercial spectrophotometer (Perkin Elmer, UV win Lab) equipped with an integrating sphere. Steady state PL measurements were carried out using a 405 nm external laser as an excitation source and a single grating monochromator (Triax 550) coupled to a cooled CCD detector (Jovin Yvon). TR PL measurements were carried out in a picosecond time resolved luminescence spectrometer (Edinburg Instruments, FSP920). EPR measurements were performed with a JEOL (JES-FA200) instrument operating in the X band. TGA data were obtained with a STA7200 HITACHI (Thermal analyser) with a heating rate of 5 °C/min by purging the high purity O₂ gas. FTIR spectroscopy measurement was performed with a commercial spectrometer (Perkin Elmer, Spectrum BX).

### 2.3. Photocatalytic experiments

#### 2.3.1. Photodegradation of methylene blue

Visible light photocatalytic studies were performed with a Xe arc lamp (ORIEL Instruments, USA) fitted with an external UV cutoff filter (Hoya Filter, Japan) and a mirror for beam reflection. MB was chosen as a model dye organic pollutant. 20 mg of catalyst was mixed with 100 mL of aqueous solution with an initial MB concentration of 8 mg/l. MB with catalyst was stirred in dark for 1 h to reach the adsorption-desorption equilibrium between dye and catalyst. Next, the solution was irradiated with visible light. During the irradiation of light, cold water was circulated to maintain the temperature of the system. At an interval of 10 min, 5 mL aliquot was taken out and centrifuged. Photodegradation of MB was measured from the UV–vis absorption spectrum of its maximum absorption peak at 665 nm after each 10 min of irradiation.

#### 2.3.2. Free radicals scavenger test

To determine the contribution of reactive species that are involved

in the photodegradation of MB, we have performed the free radical scavenger experiment. For this experiment, Ammonium oxalate (AO), tert-butyl alcohol (t-BA) and p-benzoquinone (BQ) scavengers were used to study the influence of hole ($h^+$), hydroxyl radical ($\cdot OH$) and superoxide radical ($O_2^{\circ-}$), respectively. In each experiment, 1 mM of scavenger is added to the catalyst–dye solution (20 mg, 8 mg/l) [48]. Afterwards, the dye-catalyst-quencher solution was irradiated with the Xe arc lamp fitted with an UV cut off filter (Hoya Filter, Japan). The irradiation time, sample collection and UV–vis absorption measurements conditions are identical to that mentioned in the previous section.

### 2.4. Computational methodology

In order to support the experimental results and the conclusions thereof, theoretical calculations were carried out by CASTEP code based on density functional theory (DFT) in Materials Studio program [49]. The exchange correlation interaction is implemented by generalized gradient approximation (GGA) functional in Perdew and Burke and Ernzerhof (PBE) format, using the ultrasoft pseudopotentials [50,51]. Grimme dispersion corrected density functional theory (DFT-D) has been employed for the interaction of GQD and $TiO_2$ surface. The system contains hybrid structure of a $2 \times 2$ supercell of $TiO_2$ (110) surface with two oxygen vacancies and overlapping GQD of size $1.27 \times 1.27$ nm$^2$ with oxygen functional groups. The GQD contained nine hexagonal rings with two epoxy functional groups out of the GQD plane. A vacuum space of 20 Å is placed to avoid the interaction between the adjacent layers in the direction perpendicular to the GQD plane. Geometry optimization of hybrid structure is performed until the maximum force was less than 0.05 eV/Å. We have calculated the absorption spectrum of bare anatase $TiO_2$ (110) and oxygen deficient $TiO_2$-GQD hybrid structures. Spin unrestricted calculation is performed with the Brillouin zone integration by setting an $3 \times 3 \times 2$ Monkhorst-Pack k-point grid for geometry optimization and optical properties. The cut off energy of 600 eV is used with $2 \times 10^{-5}$ eV/atom SCF convergence tolerance limit. Note that 0.1 eV smearing is used for the calculation of the absorption spectrum in each case. Computational results are compared with that of the experimental results of bare $TiO_2$ and hybrid structures.

## 3. Results and discussion

### 3.1. XRD and HRTEM studies

The structural and morphological properties of bare and hybrids of GQDs and $TiO_2$ NPs are studied by XRD and TEM analyses. Fig. 1 shows the XRD pattern of T0/GQD and T16/GQD. XRD pattern for T0 and T16 samples are provided in Fig. S1 (Supporting Information). The XRD pattern shown in Fig. 1 matches with the characteristic reflection peaks of anatase $TiO_2$ and hexagonal graphitic structure of GQDs. In the hybrid samples, the most intense peak at 2θ~25° corresponds to the anatase phase (101) plane of $TiO_2$ and another intense peak at 2θ~26.3° is originated from the (002) plane of hexagonal sp$^2$ hybridized carbon in GQDs. The (002) peak is very intense for the hybrid sample prepared with equal weight ratio of $TiO_2$ and GQDs. These results indicate the successful preparation of $TiO_2$-GQD hybrids with crystalline phases. Interestingly, in addition to the anatase $TiO_2$ phase, XRD data show two new peaks appearing at 2θ~31.28 and 41.6°, which correspond to the ($\bar{1}$12) and (312) planes of $Ti_3O_5$ (JCPDS No. 74-0819), respectively [47]. Note that the XRD peaks related to the anatase $TiO_2$, $Ti_3O_5$ and GQDs are labelled with the '●', '*' and '♦' symbols, respectively in Fig. 1 and Fig. S1 (Supporting information). It is noted that as compared to T0, the crystallinity of T16 is reduced, presumably due to the mechanical milling that causes high density of defects/disorder in the system (see Fig. S1, Supporting information). In particular, high density of oxygen vacancies are introduced during ball milling of the $TiO_2$
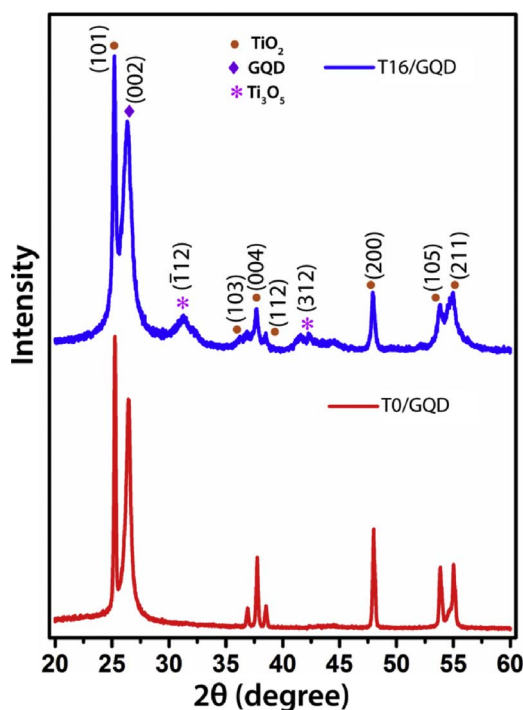


**Fig. 1.** XRD pattern of T0/GQD and T16/GQD hybrids. Note that the peaks corresponding to the anatase $TiO_2$, $Ti_3O_5$ and GQDs are shown with different symbols.

powder [47]. The role of oxygen vacancies in the formation of $TiO_2$-GQD hybrid is discussed later.

The size and morphological features of the $TiO_2$ NPs, GQDs and their hybrids were analysed by TEM and HRTEM imaging, as displayed in Fig. 2(a–i). Fig. 2(a) shows the TEM image of T0 and the average $TiO_2$ particle size is ∼80 nm. Fig. 2(b) represents the HRTEM lattice image of T0 showing a lattice spacing (d) of 3.25 Å, which corresponds to the $TiO_2$ (101) planes. Fig. 2(c) shows the TEM image of GQDs and the average size of GQDs is ∼5.2 nm. The inset shows the SAED pattern for GQDs confirming the sp$^2$ hybridized, hexagonal graphitic structure. Fig. 2(d) represents the TEM image of T16 sample and the inset shows the HRTEM lattice image, where the lattice spacing (d) 3.29 Å corresponds to the $TiO_2$ (101) plane. The lattice spacing in T16 is marginally higher than that of the T0, due to the tensile strain [47] in the $TiO_2$ NPs caused by ball milling. The formation of $TiO_2$/GQD hybrid is noticeable from the TEM/HRTEM images shown in Fig. 2(e–h) for T0/GQD and T16/GQD. Fig. 2(e) shows the TEM image of T0/GQD and the inset shows a portion of the image at a higher magnification. Uniform decoration of the GQDs on the surface of the $TiO_2$ NPs is clear from the inset image. Fig. 2(f) shows the HRTEM lattice image of T0/GQD sample, where the lattices of both $TiO_2$ and GQDs are discernible. Similarly, the GQD distribution over the T16 surface in T16/GQD hybrid can be clearly seen from the TEM images in Fig. 2(g,h). Fig. 2(g) and (h) show the TEM and HRTEM lattice image of T16/GQD. The simultaneous presence of both $TiO_2$ and GQD lattices are evident from the image and it reveals the strong attachment of the GQDs over the $TiO_2$ surface. Note that in HRTEM lattice images of $TiO_2$-GQDs hybrid in Fig. 2(f, h), the GQDs are shown with dotted circles. TEM image of T16/GQD hybrid after three repeated cycles of photocatalysis is shown in Fig. 2(i), which reveals the stable structure of the hybrid after photocatalysis experiment. These results clearly demonstrate the formation of $TiO_2$/GQD hybrid nanostructure.

### 3.2. Raman spectroscopy studies

Raman spectroscopy is an established tool for the characterization of semiconductor nanostructures and graphitic materials. In particular,
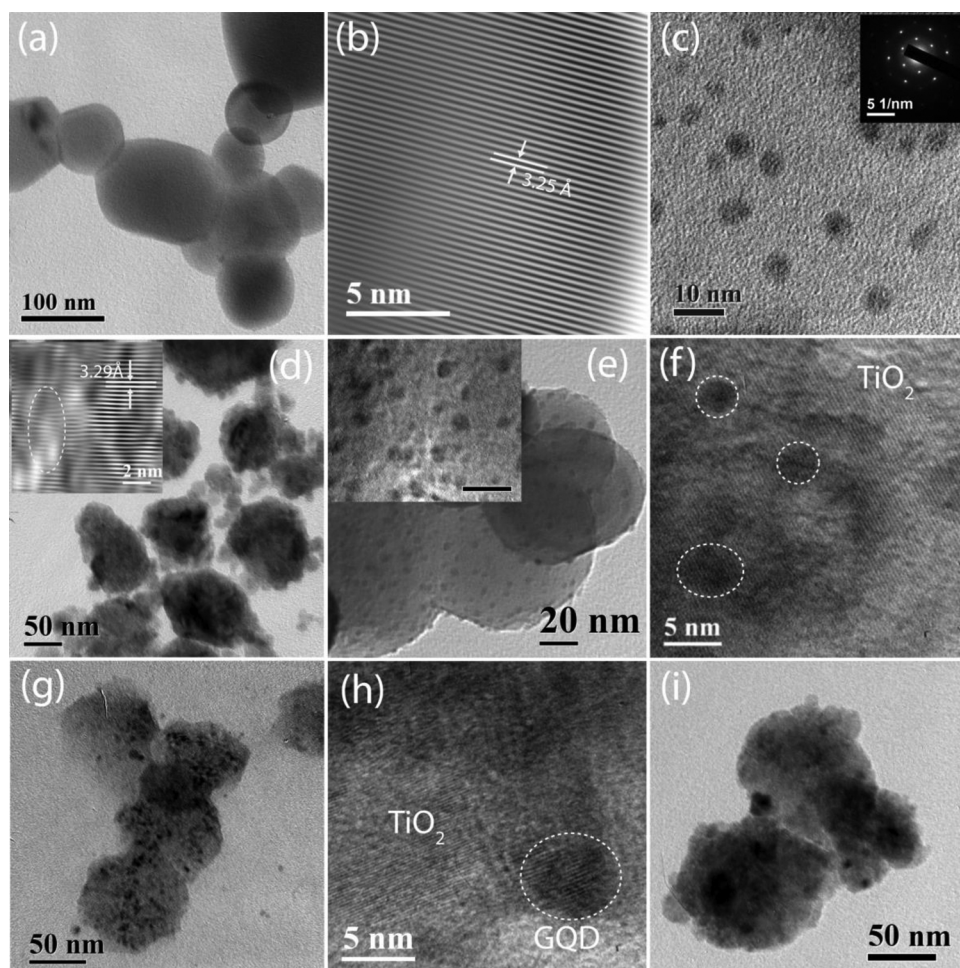
**Fig. 2.** (a, b) TEM and HRTEM lattice images of $TiO_2$ nanoparticles in sample T0. (c) TEM image of GQDs showing an average size of ~5.2 nm. The inset shows the corresponding SAED pattern. (d) TEM image of $TiO_2$ NPs in T16. The inset shows the HRTEM lattice image of single $TiO_2$ NP with the strained region marked with oval shaped dotted line. (e-f) TEM and HRTEM lattice images of T0/GQD hybrid, respectively. The inset in (e) shows the high magnification image of small GQDs on a $TiO_2$ NP surface; the scale bar is 10 nm. (g) The TEM image of T16/GQD hybrid, (h) the HRTEM lattice image of T16/GQD showing simultaneous presence of $TiO_2$ and GQDs lattices. Note that the GQDs are shown with the dotted line in (f, h). (i) TEM image of T16/GQD hybrid after 3 cycles of photocatalysis experiment.
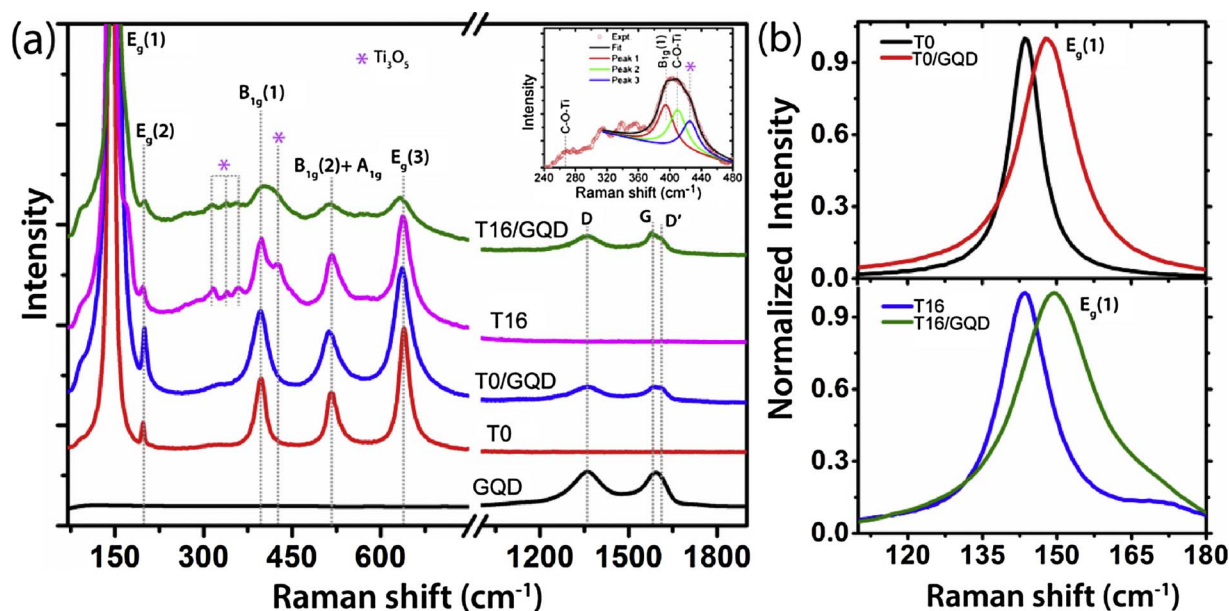


**Fig. 3.** (a) Characteristic Raman spectra of $TiO_2$ NPs and GQDs and their hybrid samples. The characteristic Raman signatures of anatase $TiO_2$ and GQDs are labelled by standard notations. Note that the curves are vertically shifted for clarity. The inset shows the magnified view of the spectrum with fitting in the region 240–480 $cm^{-1}$ for T16/GQD showing C–O–Ti modes, besides the other modes. (b) Comparison of the Raman $E_g$ (1) peak profile for the T0 and T16 samples before and after decoration of GQDs.

it provides valuable information about the crystallinity/disorder, degree of hybridization, defects and the extent of chemical modification in hybrid structures [52–55]. Fig. 3(a) shows the Raman spectra of pristine and hybrid samples of $TiO_2$ and GQDs. All the $TiO_2$ and $TiO_2$/GQD hybrid samples display the characteristic Raman bands of anatase $TiO_2$, such as three $E_g$, two $B_{1g}$, and one $A_{1g}$ modes, which are
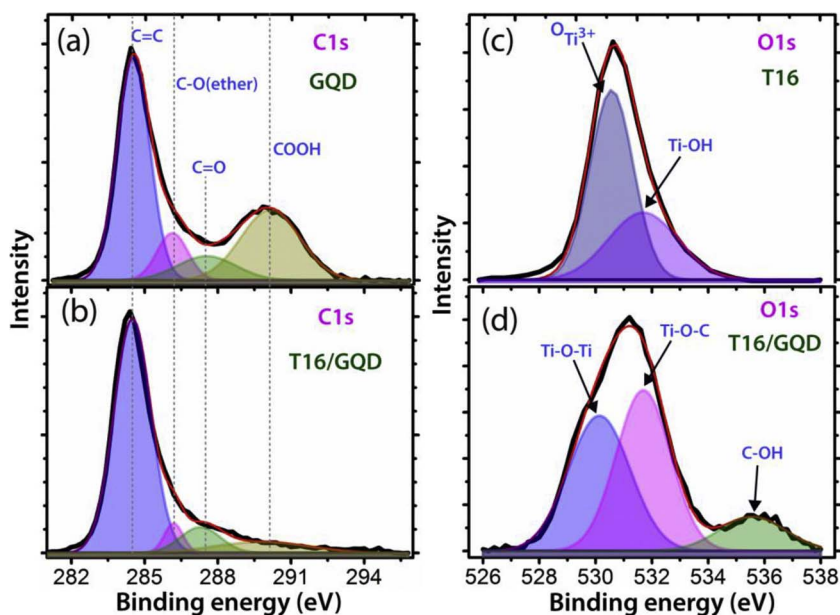
Fig. 4. Core level XPS spectra of different samples: (a–b) C1s spectra for GQD and T16/GQD, (c–d) O1s spectra for T16 and T16/GQD, respectively.

consistent with the literature reports [54,55]. In case of GQDs, the characteristic Raman G band originates from the in-plane ($E_{2g}$) vibration of $sp^2$ hybridized carbon atoms, whereas the D band arises from the edge states in graphene and it is very significant in GQDs due to availability of large density of edge carbon atoms as compared to the in-plane atoms. Based on the intensity of D band, one can determine the type of edge configuration. The D band is prominent for the armchair edges, but absent for the zig-zag edges of GQDs [56–59]. Besides the D band, another defect band, known as the D' band, appears as result of crystalline defects, such as vacancies, pentagon/heptagon or so called S-W defects [19,52]. Besides the characteristic Raman features of anatase $TiO_2$ and GQDs as labelled in Fig. 3(a), additional peaks with low intensity (marked with * symbol) related to the phase of $Ti_3O_5$ are present in T16 and T16/GQD samples. This is consistent with the XRD analysis. Previous Raman studies on hybrid structure based on $TiO_2$ and TiC indicate that Raman modes for the C−O−Ti bonds lie at ∼ 264, ∼ 407 and ∼ 620 $cm^{-1}$ [60]. In the present study, we find additional bands related to $Ti_3O_5$ and C−O−Ti bonds in T16/GQD hybrid system, after deconvolution of the Raman spectrum in the range 350–480 $cm^{-1}$. The inset in Fig. 3(a) shows a magnified view of the Raman spectrum with Lorentzian peak fitting of T16/GQD in the region 240–480 $cm^{-1}$, where the new peaks related to C−O−Ti bonds are marked at 267 $cm^{-1}$ and 410 $cm^{-1}$ [60]. Thus, the Raman results indicate the possible presence of C−O−Ti bonds in T16/GQD hybrid. This is in addition to the $B_{1g}(1)$ and $Ti_3O_5$ modes (denoted by "*" symbol) present in the hybrid system. Note that in case of $TiO_2$-GQD hybrid, due to the introduction of possible additional covalent bond (e.g., C−O−Ti), lattice strain may be introduced resulting in broadening in Raman line shape (see Fig. 3(b)).

The linkage of oxygen deficient $TiO_2$ and GQD through the possible C−O−Ti bonds can be understood by the blue shift of $E_g(1)$ Raman mode in the hybrid samples. Fig. 3(b) shows a comparison of the Raman $E_g(1)$ peak profiles of $TiO_2$ and $TiO_2$-GQD hybrid samples. The centre of the Raman $E_g(1)$ for T0/GQD and T16/GQD are at 148.0 and 149.8 $cm^{-1}$, respectively, which are upshifted by 5 and 6 $cm^{-1}$ from that of the T0 and T16. The shift in $E_g(1)$ peak in T16/GQD is 1.8 $cm^{-1}$ higher than that of T0/GQD. These results indicate a strong interaction between GQD and $TiO_2$ through defects in $TiO_2$. The shift in the Raman peak in hybrid samples is possibly due to the formation of C−O−Ti− bond, when GQD and $TiO_2$ come in contact with each other or due to the strain.

With the first principle calculations, Long at el. proposed that the central part of GQDs is mostly intact with $TiO_2$ surface and resultant GQDs is slightly bent [27]. We believe that the central part, most likely the in-plane epoxy functional groups, is directly connected to the defect sites in $TiO_2$ possibly through the C−O−Ti bonds after the hybrid formation, which is supported by our simulation results (discussed later). As a result, the in-plane part of GQD is more favourable to form the hybrid with $TiO_2$. These results further indicate the change in the oxygenated functional groups, without significant change in the edge configuration. To estimate the relative contribution of in-plane functional groups and edge states, we calculate the intensity ratio of Raman D band to G band ($I_D/I_G$) in GQDs and $TiO_2$-GQD hybrid. The $I_D/I_G$ ratios are 1.08, 1.01 and 0.97 for GQDs, T0/GQD and T16/GQD, respectively. The negligible change in $I_D/I_G$ ratio for different samples indicates the uniform edge configuration of GQDs. It is important to note that despite the formation of the $TiO_2$-GQD hybrids, the edge sites (zig-zag and armchair) configuration of GQDs is unaltered [36]. This implies that the changes take place mostly at the in-plane oxygenated functional groups of GQDs. The oxygenated functional groups may have been formed during the ultrasonication to facilitate the hybrid formation [61]. We speculate that in the present case the edge and in-plane oxygenated functional groups are re-distributed and provides the in-plane disorder (in-plane epoxy C−O) to facilitate the hybrid/junction formation. The basal plane disorder in GQDs is directly linked to the bonding of $TiO_2$ with the GQDs through the linking of basal plane C−O to the Ti in $TiO_2$.

It may be noted that the stability of edge sites in GQDs is higher than that of the edge oxygenated functional groups. Note that our XPS results (discussed below) suggest the decrease in some of the edge oxygenated functional groups after hybrid formation. As a result, the oxygen functional groups in GQDs can rearrange due to its weak bonding. Note that the ratio of in-plane to edge carbon atoms is relatively small in GQDs as compared to that of graphene oxide. Thus, we believe that the ultrasonication induced in-plane epoxy disorder enables the possible formation of the C−O−Ti bonds in $TiO_2$-GQD hybrid. In order to form such C−O−Ti− bonds, some of the functional groups might be supplied from the atmosphere during the hybrid formation [61].

### 3.3. XPS studies

In ordered to understand the chemical composition and bonding environment in different samples, XPS measurements were conducted. Fig. 4(a,b) represents the core level C1s spectra for GQD and T16/GQD.

The C1s spectrum is fitted with four Gaussian peaks centred at 284.5 (P1), 286.1 (P2), 287.5 (P3) and 290.1 eV (P4). The peak P1 signifies the honeycomb lattice structure of $sp^2$ hybridized carbon atoms, whereas the other peaks (P2, P3, and P4) correspond to the oxygen related edge functional groups in GQDs, such as C−O (ether), C=O, and COOH, respectively [19,62]. It is evident from the fitted data that the C−O (ether) and COOH functional groups are significantly reduced in the hybrid sample, which implies that some of the oxygen related functional groups may be converted to in-plane epoxy group to facilitate the possible formation of C−O−Ti bonds in the TiO$_2$-GQD hybrid. The edge carbon atoms are bonded with C−O (ether), COOH and C=O oxygen functional groups, among which the C=O is highly stable [19,63]. Due to less stability, the C−O (ether) and COOH functional groups may relocate during the hybrid formation. Note that we have not noticed any Ti−C bond related peak in the C1s XPS spectrum of T16/GQD. This further implies that the Ti and C are bonded through the oxygen atom in ordered to form the possible C−O−Ti bonds. Note that some studies indicated the Ti−C bond formation in TiO$_2$ and carbon hybrid [37,64]. Further, the change in surface states in T16 and T16/GQD samples is understood from the core level O1s XPS spectra, as shown in Fig. 4(c,d). Based on the nature of the O1s XPS spectrum, the XPS spectrum of T16 is fitted with two Gaussian peaks centred at 531.1 and 532.2 eV, which are attributed to the Ti−O bonds (O$_{Ti}^{3+}$) and organic impurities, respectively [37,65]. In contrast, the O1s XPS spectrum of T16/GQD shows asymmetry and distinctly different peaks. Accordingly, the XPS spectrum is fitted with three Gaussian peaks. The peak centred at 530.1 eV is referred to the oxygen in crystal lattice (O$_L$) [65] and the other two peaks at 531.7 and 535.5 eV are due to the Ti−O−C and hydroxyl functional group (C−OH) [37,66], respectively. The XPS peaks in the range 530.0-532.1 eV are assigned to the Ti−O−C bond in the literature [7,36,37]. In the present case, the strong peak at 531.7 eV is believed to result from the Ti−O−C bond. These results indicate the hybrid formation in TiO$_2$-GQD possibly through the Ti−O−C bonds. The core level Ti 2p XPS spectra of T16 and T16/GQD are provided in Fig. S2 (Supporting information). The peaks in the range ∼ 458.1-458.3 eV and ∼ 463.8-464.0 eV are due to the Ti 2p$_{3/2}$ and 2p$_{1/2}$ orbital splitting of Ti 2p core level states in TiO$_2$ [65].

### 3.4. UV–visible absorption and FTIR studies

The UV–vis absorption characteristics of the T0, T16 and T16/GQD samples are depicted in Fig. 5. Fig. 5 shows the Kubelka-Munk plots (absorption spectra) for T0, T16 and T16/GQD samples obtained from the diffused reflectance spectrum of the respective samples. The band edge of T16 is clearly red shifted with respect to that of the T0, due to
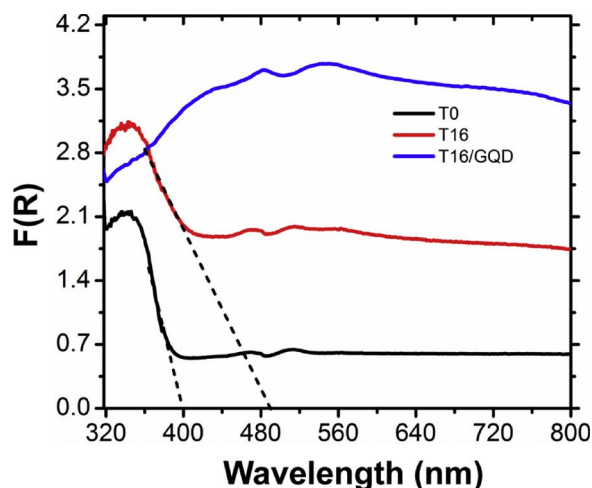


**Fig. 5.** Kubelka-Munk plot (F(R)) of absorbance derived from diffuse reflectance spectra of T0, T16 and T16/GQD samples in the powder form.

the combined effect of strain and oxygen vacancy defects, as reported in our previous study [47]. This clearly implies a narrowing of the band gap in the T16 sample. Further it shows enhanced absorption in the visible region as compared to that of T0. Interestingly, the T16/GQD hybrid sample shows very strong absorption in the entire visible to near-infrared (NIR) region. This extended range absorption is highly advantageous for the visible-NIR light photocatalysis and related applications. This extended absorption is due to the hybrid formation through the coupling of GQDs to TiO$_2$ possibly via C−O−Ti covalent bonds. An intimate contact between the TiO$_2$ and GQDs through this bond facilies the efficient interfacial charge transfer from GQDs to the TiO$_2$ [27]. Note that GQDs have some visible absorption, besides the strong UV absorption, as shown in Fig. S3(a). The π-π* and n-π* transition peaks appeared at ∼ 269 and ∼ 332 nm are due to the $sp^2$ carbon domains and functional groups defects in GQDs, respectively [19].

The characteristics of anatase TiO$_2$ and formation of TiO$_2$/GQD hybrid is further confirmed from the FTIR analysis. Fig. 6(a) shows the FTIR spectra for T16 and T16/GQD. The TiO$_2$ vibrational modes lying in the range 600–800 cm$^{-1}$ can be attributed the Ti−O and O−Ti−O bonds [41,65]. Note that in T16/GQD, the O−Ti−O vibrational peak is shifted to lower wavenumber as compared to that of T16. This red shift is a signature of the formation of hybrid possibly through the C−O−Ti−bond formation [41]. In addition, a vibrational band at ∼ 1400 cm$^{-1}$ is observed in T16 and it is due to the Ti−O−Ti vibration in TiO$_2$ [67]. Notably, this mode becomes prominent in GQDs/T16 probably due to the lattice distortion caused by the formation of possible C−O−Ti−bond or oxygen vacancy rearrangement during the hybrid formation. The peak at 1620 cm$^{-1}$ in T16 is could be due to the adsorption of water/OH on TiO$_2$ [68], whereas two weak vibrational modes at 1590 and 1650 cm$^{-1}$ in T16/GQD are due to the C=C and COOH bonds, respectively [19,69]. These results confirm the presence of GQDs in hybrid sample. Interestingly, we observed an additional broad band centred at ∼ 2131 cm$^{-1}$ in T16/GQD sample, as shown in the inset of Fig. 6(a). Based on the literature reports, this band is attributed to the C−O−Ti bond (C−O attachment at oxygen deficient sites in TiO$_2$) [70]. From this result, it is believed that the oxygen in GQDs may bind to the oxygen deficient sites in TiO$_{2-x}$, which results in the possible formation of C−O−Ti bonds in the T16/GQD hybrid samples. A broad vibrational band in the range from 3000 to 3900 cm$^{-1}$ is due to OH vibrations [19,41].

### 3.5. PL and TRPL studies

#### 3.5.1. Steady state PL

To understand the nature of defects and their role in hybrid formation, we have carried out the PL measurements on the pristine and hybrid samples. The PL spectra of T0, T16, GQD and T16/GQD obtained with 405 nm laser excitation are portrayed in Fig. 6(b). The broad PL spectrum from T0 and T16 is as a result of transition of electrons from different defect states; particularly the green PL emission (∼ 520 nm) is due to oxygen vacancy defects in TiO$_2$ [65]. Note that the PL intensity of T16 is substantially higher than that of the T0 due to the introduction of additional oxygen vacancy defects during the ball milling process [47]. On the other hand, PL spectrum of GQDs shows strong blue-green emission; the blue PL emission arises from the edge states and the green PL emission arises from the oxygenated functional groups in GQDs [19,62,71]. Interestingly, the PL spectrum of T16/GQD shows a much lower intensity than that of the individual components. In particular, the intensity of green PL emission is significantly reduced as compared to that of the blue PL in the hybrid sample. For T16/GQD hybrid, the green PL (∼ 518 nm) intensity is 5.6 times lower than that of pristine T16. This may indicates the reduction/passivation of oxygen vacancies in the hybrid system due to the bonding of GQDs to oxygen vacant sites in TiO$_2$, possibly through the C−O−Ti bonds. The partial quenching of PL intensity is also indicative of the electron transfer from GQDs to TiO$_2$. In order to ascertain that the additional oxygen vacancies are
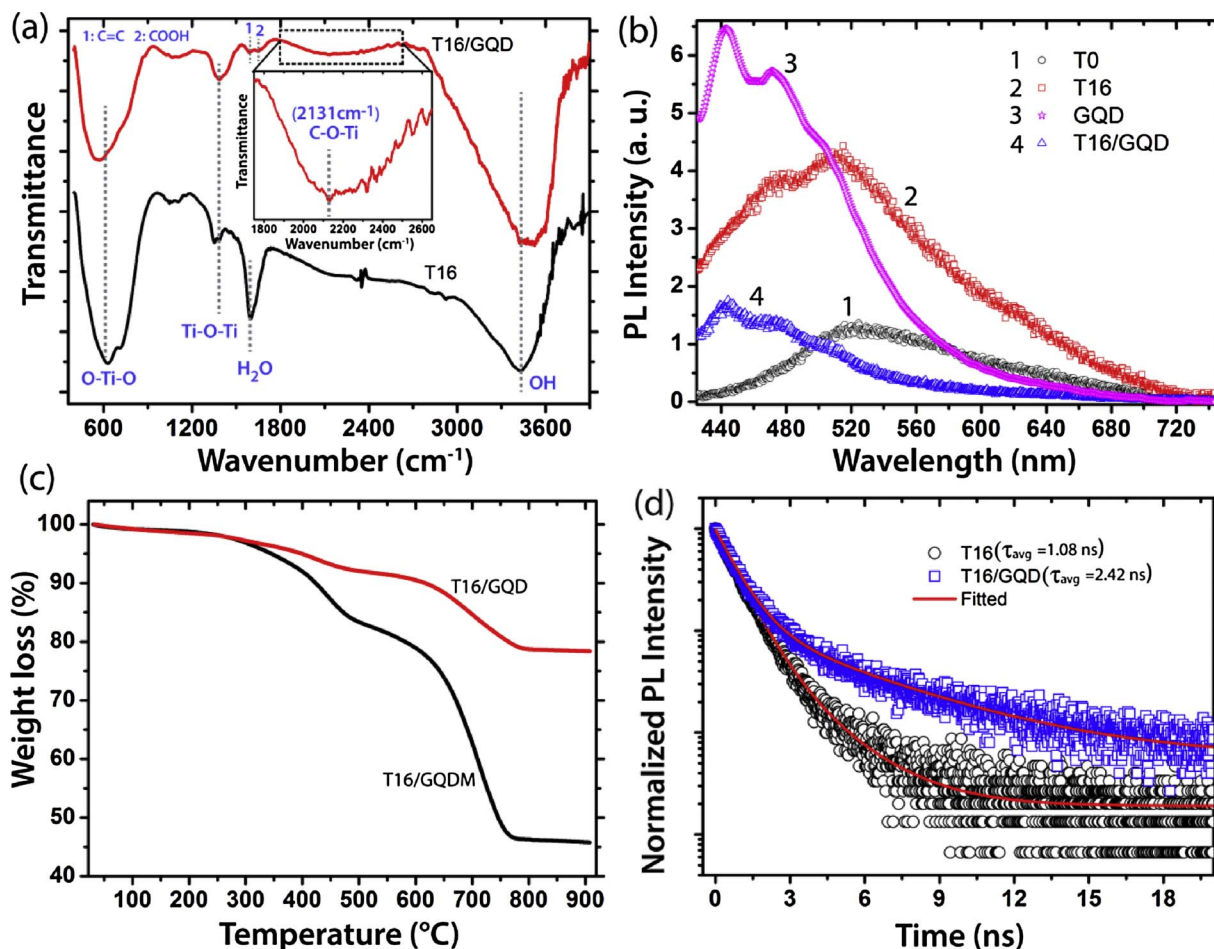
**Fig. 6.** (a) Comparison of FTIR spectra for T16 and T16/GQD. The inset shows the magnified view of a portion of the spectrum showing the presence of C−O−Ti bonds. (b) Comparison of PL spectra excited with 405 nm laser for T0, T16, GQD and T16/GQD hybrid showing reduced PL intensity in the hybrid sample. (c) Comparison of TGA profiles of T16/GQD and T16/GQDM showing higher thermal stability of T16/GQD. (d) TRPL spectra excited with 405 nm pulsed laser for T16 and T16/GQD showing longer life time of photo-generated carriers in the hybrid sample.

indeed formed during the ultrasonication, we compare the PL intensities of sample T0 before and after ultrasonication (T0S), as shown in Fig. S3(b) (Supporting information). It's evident that the visible PL intensity of T0 is increased by four fold after ultrasonication, which implies the creation of additional oxygen vacancies during the ultrasonication of bare $TiO_2$ NPs.

### 3.5.2. TGA analysis

In order to ascertain the role of oxygen vacancies in the hybrid formation, we prepared two different hybrid samples: (i) mixing of GQDs and $TiO_2$ under simple stirring (T16/GQDM), and (ii) mixing of GQDs and $TiO_2$ under ultrasonication (T16/GQD). Interestingly, the TGA analyses of these two samples showed quite different weight loss characteristics due to the difference in hybrid formation. Fig. 6(c) shows the TGA profiles of T16/GQDM and T16/GQD. The results can be understood as follows. In case of the hybrid prepared under stirring (T16/GQDM), the faster weight loss characteristics indicates that the GQDs may be loosely attached to the $TiO_2$ surface, perhaps physisorbed onto the $TiO_2$ surface due to insufficient energy to change local structure (e.g., oxygen vacancies) in $TiO_2$, and negligible rearrangement in the functional groups in GQDs. On the other hand, in case of the hybrid prepared by ultrasonication (T16/GQD), the slower and low weight loss characteristic indicate strong bonding between the $TiO_2$ and GQDs through some changes in the local structure (e.g., oxygen vacancies) in $TiO_2$ and functional groups rearrangement in GQDs. It is likely that the in-plane epoxy (C−O) functional groups in GQDs are transferred to the oxygen deficient sites in $TiO_2$ and form a hybrid possibly through the

C−O−Ti bonds. This type of bond strongly couples the GQDs and $TiO_2$. Thus, ultrasonication of the hybrid mixture results in a kind of chemisorption of GQDs on to $TiO_2$, instead of physisorption. The chemisorption is believed to be responsible for the high thermal stability and low weight loss (only ~20%) in T16/GQD. These results clearly demonstrate the role of oxygen vacancies in $TiO_2$ in the formation of $TiO_2$/GQD hybrid. Note that T16 contains high density of oxygen vacancies and during ultrasonication, more vacancy sites of $TiO_2$ are available for chemisorption of GQDs with in-plane C−O functional groups and it results in the hybrid formation with covalent bonding. It is likely that the hybrid sample prepared only under stirring leads to the van der Waals interactions between GQD and $TiO_2$, which is likely to yield physisorption.

### 3.5.3. Time resolved PL

To gain further insight into the mechanism of the interfacial charge transfer in $TiO_2$-GQD hybrid, we performed the TRPL measurements on T16 and T16/GQD. For the TRPL measurements, the samples are excited with the 405 nm laser source and the PL emission is monitored at 518 nm, based on the steady state PL spectrum. Fig. 6(d) shows the TRPL spectra for T16 and T16/GQD. Each spectrum is well fitted with a bi-exponential decay, indicating that two life time components contribute in the carrier dynamics. The carrier life time values for T16 are 0.82 ($\tau_1$) and 2.08 ns ($\tau_2$), possibly due to the prompt recombination of charge carries from defect states in $TiO_2$. On the other hand, the carrier life time values for T16/GQD are 0.82 ns ($\tau_1$) and 4.5 ns ($\tau_2$), indicating a slower decay in the hybrid sample. The average life time values in T16

and T16/GQD are 1.08 and 2.42 ns, respectively. This prolonged life time value in the hybrid sample signifies the efficient charge separation at the TiO$_2$-GQD interface. These separated charge carriers play a vital role in the free radical generation and dye degradation process, which is illustrated later. These results are consistent with the steady state PL analysis, which showed lower PL intensity in the hybrid sample. Our results are fully consistent with the theoretical calculations reported by R. Long [27]. Through density functional theory calculations, R. Long [27] reported on the efficient electron transfer and charge separation at the TiO$_2$/GQD interface where the GQDs were chemisorbed on to TiO$_2$ (110) surface. The report also suggested that visible light irradiation can excite the electrons of GQD to be injected into the TiO$_2$ surface due to band-gap narrowing of GQD/TiO$_2$ composites relative to pure TiO$_2$ [27].

### 3.6. EPR studies

In ordered to understand the nature of defects in pristine and TiO$_2$-GQD hybrid, we have performed the EPR measurements. Fig. S4 (Supporting information) shows the EPR spectra of T16, GQD and T16/GQD samples. The intensity of EPR signal for T16 is very high as compare to other samples, which could be due to the large density of defects in T16 [72]. This result is consistent with the PL analysis, which showed high density of oxygen vacancy defects in T16. The EPR signal at g value 1.9905 is due to the oxygen defects related to the F$^+$ centres in TiO$_2$ [72]. On the other hand, the EPR signal at g value 1.9975 in GQD is due to the free electron sites (edge states) [73]. The possible reason for lower g-value and reduction of EPR intensity in the GQD sample could be due to the large density of oxygenated functional groups attached at the edge sites of carbon. Presence of various functional groups such as −OH, −CO, and −O etc. in GQDs strongly influence the EPR signal [73]. Note that broad PL (blue-green) emission from GQDs (see Fig. 6(b)) results from the edge states and functional groups, as discussed above. In addition, our XPS studies of GQDs further supports the evidence for edge oxygenated functional groups. Thus, the results of XPS and EPR analysis are consistent with each other. In hybrid sample, the g-value of 1.9961 is due to the F$^+$ centres in TiO$_2$ [72]. Interestingly, in case of T16/GQD, the EPR signal intensity is reduced, possibly due to passivation of the defects in TiO$_2$ by the GQDs. Note that we observed reduced intensity of peaks related to functional group in XPS C1s spectrum of the hybrid sample. Thus, the reduced EPR signal indicates the formation of TiO$_2$-GQD hybrid possibly due to C−O−Ti covalent bonding. These results are consistent with the PL analysis of the hybrid sample.

### 3.7. Computational study on the optical spectra of TiO$_2$/GQD hybrid

In ordered to verify the physical validity of possible C−O−Ti bonds for the hybrid formation and to compute its corresponding optical spectra, we have performed the DFT calculations on the anatase TiO$_2$ and oxygen deficient TiO$_2$-GQD hybrid structures. The atomistic structures of the bare TiO$_2$ and TiO$_2$-GQD hybrid without and with energy optimization are shown in Fig. 7(a–c). The corresponding optical absorption spectra for different structures are shown in Fig. 7(d). Interestingly, as compared to bare the TiO$_2$, the oxygen deficient TiO$_2$-GQD hybrid without and with optimization show much stronger absorption in the visible region and the absorption tail is extended to NIR region. The computed absorption spectra are fully consistent with our experimental absorption data shown in Fig. 5. Our results are quite consistent with the literature report on TiO$_2$-graphene hybrid, where a red-shift of absorption edge and greatly improved absorption intensity in the visible region was reported [74]. Thus, it is concluded that in the present case the coupling of functionalized GQD with oxygen deficient TiO$_2$ through the possible Ti−O−C bonds gives rise to extended absorption in the visible-NIR region. This results in highly improved photocatalytic performance of the hybrid under visible-NIR light

irradiation.

Based on our finding, a schematic model for the structural arrangement in TiO$_2$-GQD hybrid is presented in Fig. 8, using the *Material Studio* software. It depicts the structural changes taking place in TiO$_2$ and GQD to form TiO$_2$-GQD hybrid through possible C−O−Ti bonds during ultrasonication. Note that the edge sites in GQD contain various oxygenated functional groups, such as COOH, C−O (ether) and C=O. After ultrasonication of TiO$_2$, more oxygen vacancy defects are created, as shown in Fig. 8(a,b). The ultrasonication of the mixture of TiO$_2$ and GQD (Fig. 8(c)) results in creation of additional oxygen vacancies in TiO$_2$ and redistribution of oxygen functional groups in GQDs. The resultant hybrid structure of TiO$_2$-GQD bonded through the possible C−O−Ti covalent bonds is shown in Fig. 8(d). This is consistent with the recent report on TiO$_2$-graphene oxide hybrid by Umrao et al. [37].

### 3.8. Visible light photocatalysis studies

The oxygen vacancy mediated TiO$_2$-GQD hybrid formation, interfacial charge transfer and its influence on the visible light photo-degradation of organic dye (MB) is studied in details. Fig. 9 shows the photocatalytic degradation and kinetics of MB degradation in different catalysts. Fig. 9(a) represents the UV–vis absorption spectra of MB up to 120 min irradiation using T16/GQD catalyst. Fig. 9(b) shows the variation in concentration ratio (final to initial concentration, C/C$_0$) as a function of irradiation time for bare MB and MB in different catalyst samples subject to visible light irradiation up to 120 min. MB is only 6% self-catalysed after irradiation of 120 min. On the other hand, the degradation of MB in T16 is increased to the 44%, while it is dramatically high (97%) for T16/GQD hybrid. The photo degradation of MB in T16 is primarily due to the effect of band gap narrowing. Note that the band gap narrowing in T16 is the combined effect of strain and oxygen vacancies induced by milling process [47,75]. On the other hand, due to the band bending at the heterojunction of T16/GQD hybrid, the degradation efficiency is vastly high. We believe that the chemi-adsorption of GQDs on TiO$_2$ and the possible C−O−Ti bond formation are responsible for the efficient interfacial charge transfer and enhanced photocatalytic performance of the hybrid sample. Interestingly, our degradation studies on the T16/GQDM sample prepared by simple stirring showed only 59% degradation in contrast to the 97% degradation in case of T16/GQD. The lower degradation in case of T16/GQDM is believed to be due to the weak van der Waals interaction between the GQD and TiO$_2$ during the stirring. In contrast, during the ultrasonication, oxygen vacancy mediated bond formation takes place possibly through C−O−Ti bonding and due to strong interaction between TiO$_2$ and GQD, the efficient charge carrier separation at the interface takes place, which results in high degradation rate.

Note that besides the interfacial charge transfer process, another considerable factor is the hot charge carrier injection from GQDs to TiO$_2$ [29]. Considering the T16/GQD sample, GQDs are strongly coupled to the TiO$_2$ as compared to that in T16/GQDM. As a result, the interfacial charge separation and hot carrier generation is higher in T16/GQD as compared to that of T16/GQDM.

Next, we estimate the degradation rate constants for MB in different catalysts. The kinetics of the photocatalytic reaction followed a pseudo first order reaction process, which is expressed by $\ln(C/C_0) = k_{app}$, where $k_{app}$ is the apparent reaction rate constant, C and C$_0$ are the concentration of MB after irradiation time t and initial concentration, respectively. The rate constants are obtained from the slope of the linear plots. Fig. 9(c) shows a plot of ln (C/C$_0$) vs irradiation time for degradation of MB in the different catalysts. The rate constant for T16 is $0.46 \times 10^{-2}$ min$^{-1}$, while that of T16/GQD is $2.40 \times 10^{-2}$ min$^{-1}$ and that of T16/GQDM is $1.47 \times 10^{-2}$ min$^{-1}$. Thus, the hybrid sample shows much improved (5.2 fold higher) degradation rate constant than the pristine sample. The MB degradation (%) and the corresponding rate constants of different samples are shown in Fig. 9(d$_1$,d$_2$). These results signify the influence of interaction of GQDs and TiO$_2$ for
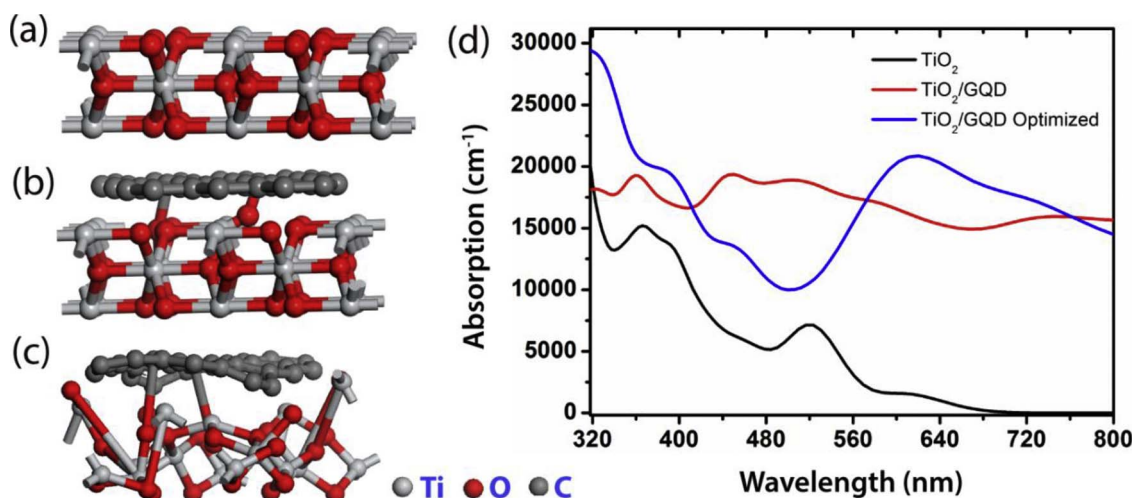
**Fig. 7.** DFT simulation images of structure of (a) anatase $TiO_2$, (b) oxygen deficient $TiO_2$-GQD hybrid without optimization, (c) optimized oxygen deficient $TiO_2$-GQD hybrid structure, and (d) Comparison of optical absorption spectrum of anatase $TiO_2$ (100) and oxygen deficient $TiO_2$-GQD hybrids.
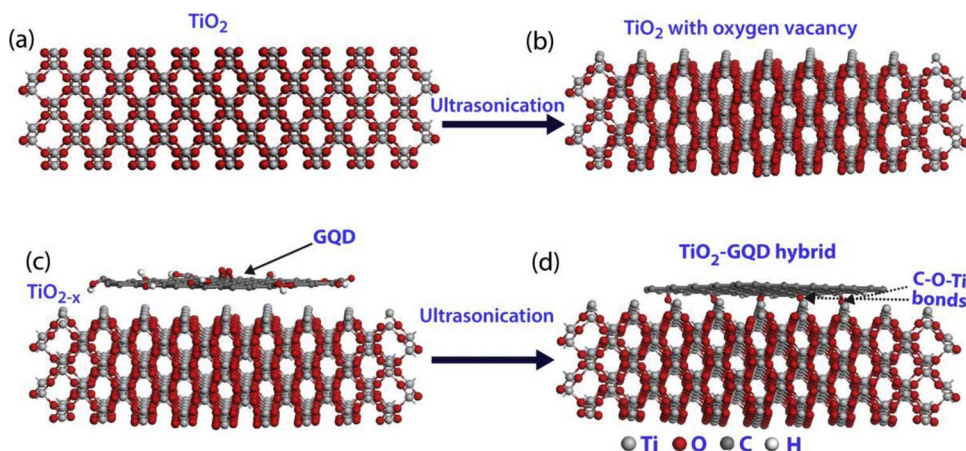


**Fig. 8.** (a, b) Schematic illustration of structural transformation in $TiO_2$ NPs by ultrasonication that creates additional oxygen vacancy defects in $TiO_2$. (c, d) $TiO_2$-GQD hybrid formation through the possible C−O−Ti bonds aided by ultrasonication of $TiO_2$ NPs and GQDs mixture. The images are simulated in _Materials Studio_ software.

enhanced photocatalytic degradation of MB. The degradation mechanism and the nature of free radical species involved in the degradation of MB are elucidated in the following section. We also studied the reusability of the T16/GQD catalyst, since it has shown the highest efficiency photodegradation of MB as compared to the other catalysts. The relative concentrations of MB in T16/GQD catalyst for three repeated cycles of photocatalysis are shown in Fig. 10(a). It's evident from the data that the hybrid catalyst is quite stable up to three repeated cycles. Further, in ordered to assess the structural stability of the catalyst, we recorded the XRD pattern of the samples before and after three cycles of catalysis. Fig. 10(b) shows the XRD pattern of T16/GQD before and after catalysis. Note that the anatase $TiO_2$, $Ti_3O_5$ phase and GQDs reflection planes are symbolized in Fig. 10(b). These results indicated that crystalline phase of the $TiO_2$ and GQD is unchanged even after three repeated cycles of photocatalysis. These results are consistent with the TEM results shown in Fig. 2(i).

### 3.9. Free radical detection and degradation mechanism of MB

In a typical photocatalysis degradation process, hole ($h^+$), hydroxyl radical ($\cdot OH$) and the superoxide radical ($O_2^{\circ-}$) are active species involved in the reactions [76,77]. To investigate and explore their contribution in visible light photocatalysis, a series of scavenger test was performed on T16/GQD catalyst. Ammonium oxalate (AO), tert-butyl alcohol (t-BA) and p-benzoquinone (BQ) scavengers were used to study the roles of hole ($h^+$), $\cdot OH$ and $O_2^{\circ-}$ radicals, respectively [76,77]. As compared to the bare T16/GQD, the degradation efficiency of MB is reduced/quenched after addition of any scavenger. This indicates the contribution of all the oxidative species to the MB degradation. Fig. 11(a) represents the evolution of the relative concentration of MB in different scavengers, and Fig. 11(b) shows the degradation (%) of MB in presence of different catalyst-scavenger combination. Note that without any quencher, the MB is degraded by 97%. It can be understood from the scavenger test that the MB is degraded by 76% in BQ, and it is quenched to 46% in t-BA. Interestingly, high quenching of MB degradation (38%) is observed in presence of AO. These results indicate the significant role of holes ($h^+$) in the MB degradation. Further, t-BA scavenger studies show the second highest quenching of MB degradation. This demonstrates that $\cdot OH$ radical is a major reactive species in MB degradation. Indeed, in the photocatalysis process the photo-generated holes are the sources for $\cdot OH$ radicals emerging. On the other hand, the electrons from GQDs are transferred to the $TiO_2$ conduction band and they trap the molecular oxygen ($O_2$) and convert it to the $O_2^{\circ-}$ radicals. This process enables efficient utilization of holes for the generation of the $\cdot OH$ radicals. The high degradation of MB in BQ can be interpreted as conversion of superoxide radical in to the $\cdot OH$ radical, as detailed below.

Based on the above results, we can discuss about the mechanism of enhanced charge separation and enhanced photocatalytic activity of $TiO_2$-GQD hybrid. Note that the $TiO_2$-GQD heterojunction forms a type-II band alignment, which is thermodynamically more favourable [28,42]. Fig. 11(c) shows a schematic representation of interfacial charge transfer and free radical generation in $TiO_2$-GQD hybrid during the photocatalysis process. The superoxide free radicals are unstable in
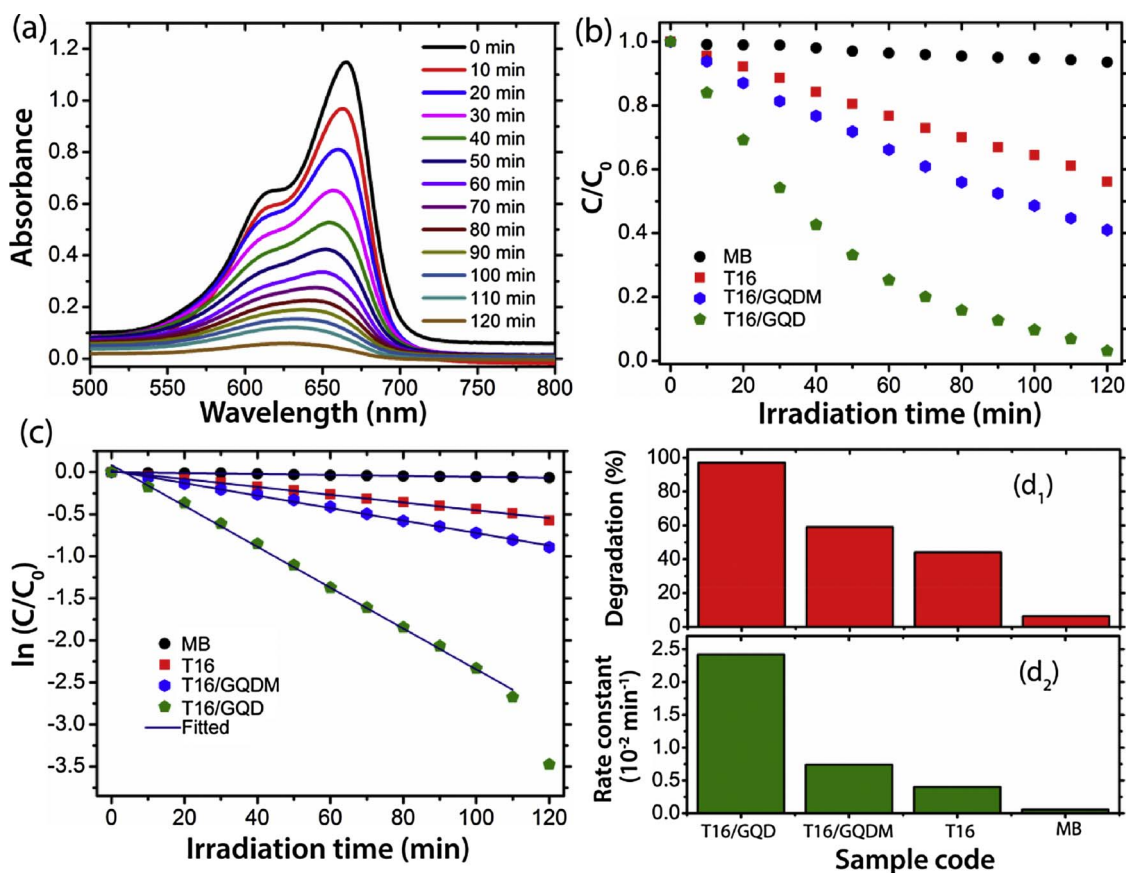
**Fig. 9.** Visible light photocatalytic degradation of MB for different catalyst samples. (a) UV–vis absorption spectra of MB in T16/GQD. (b) Change in relative concentration ($C/C_0$) of MB in different catalysts as a function of irradiation time up to 120 min. (c) Plot of $\ln(C/C_0)$ vs. irradiation time (t) for MB degradation in different catalysts. ($d_1, d_2$) Comparison of MB degradation% and first order rate constants for different catalysts, respectively.
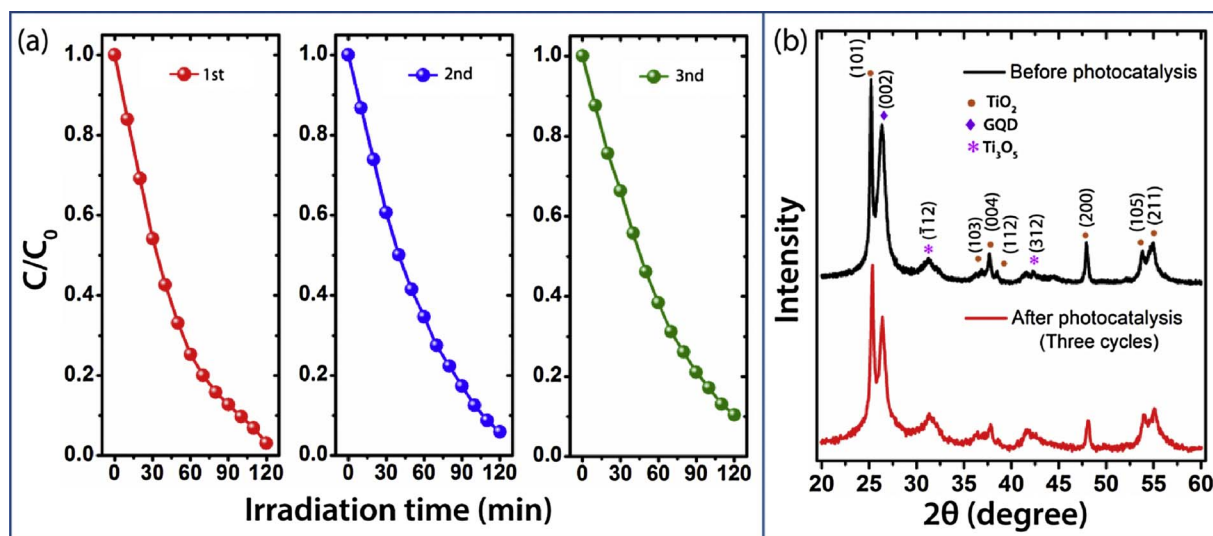


**Fig. 10.** (a) Change in relative concentration of MB as a function of irradiation time for T16/GQD catalyst for three repeated cycles. (b) XRD pattern of T16/GQD catalyst before and after three cycles of photocatalysis.

aqueous solution and these are immediately converted to the ·OH radicals [48]. Since the band gap of $TiO_2$ is narrowed in T16 as evident from the absorption spectrum, part of the visible light is absorbed by T16 and gives rise to the MB degradation up to ~44%. Note that the anatase phase of $TiO_2$ surface is more facile and versatile for generation of mobile ·OH radical [3,9]. However, the charge separation is the one of the major factor influencing the MB degradation efficiency. In case of the $TiO_2$-GQD hybrid, the band alignment at the heterojunction

facilitates the charge separation at the interface, where GQD act as a donor and the $TiO_2$ as an acceptor. Our TRPL results (Fig. 6(d)) lend strong support to the fact that there is efficient charge separation at the heterojunction giving rise to the enhanced photocatalysis. Once the charges are separated, the ·OH and $O_2^{\circ-}$ radicals are formed which are highly energetic to decompose the MB into water, $CO_2$ and other inorganic compounds. However, as compared to the superoxide radical, the ·OH radical contribution is more in the present case, as described

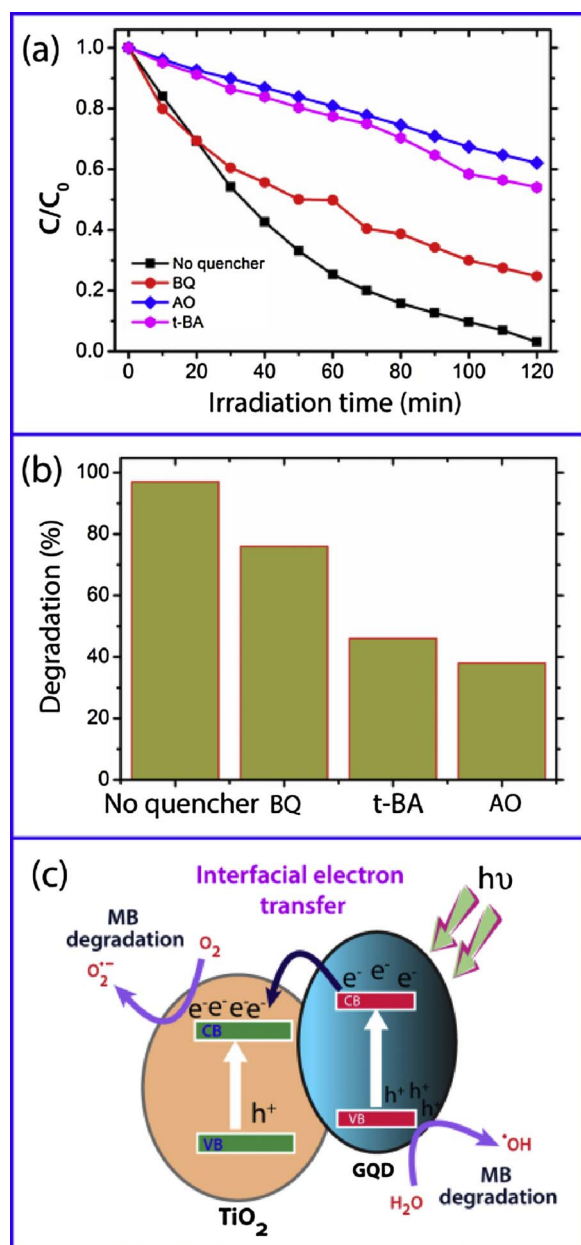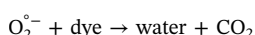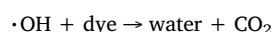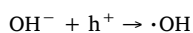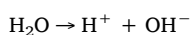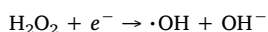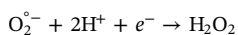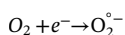**Fig. 11.** (a) Relative MB concentration as a function of irradiation time in absence and in presence of different catalyst-scavengers (scavengers: BQ ($O_2^{\circ-}$), t-BA (·OH), and AO ($h^+$)), and (b) Degradation (%) of MB in without quencher and in presence of scavengers. (c) Schematic illustration of interfacial charge separation at the TiO$_2$-GQD heterojunction and free radical generation for MB degradation.

earlier. The possible degradation pathways for MB can be expressed by the following reactions.

$$O_2 + e^- \rightarrow O_2^{\circ-}$$

$$O_2^{\circ-} + 2H^+ + e^- \rightarrow H_2O_2$$

$$H_2O_2 + e^- \rightarrow \cdot OH + OH^-$$

$$H_2O \rightarrow H^+ + OH^-$$

$$OH^- + h^+ \rightarrow \cdot OH$$

$$\cdot OH + dye \rightarrow water + CO_2$$

$$O_2^{\circ-} + dye \rightarrow water + CO_2$$

## 4. Conclusions

In conclusion, we have fabricated the TiO$_2$-GQD hybrid nanostructure by a simple ultrasonication process and studied its photocatalytic degradation efficiency for MB. With the help of various experimental tools and DFT calculation, we elucidated the mechanism of TiO$_2$-GQD heterojunction formation through the possible C−O−Ti bonds achieved by ultrasonication induced oxygen vacancy creation in TiO$_2$ and in-plane epoxy functional group rearrangement in GQDs. Our PL results further demonstrate the efficient interfacial charge transfer from GQDs to TiO$_2$ possibly through the C−O−Ti bonds. Our Raman analysis on the hybrid system revealed the strong interaction between the GQD and TiO$_2$. The FTIR, Raman and XPS analyses suggested the possible existence of C−O−Ti bonds in the hybrid system. UV–vis absorption studies show extended visible to NIR absorption in TiO$_2$-GQD hybrid system. With the help of the Raman and XPS studies, we proposed that the in-plane functional group in GQDs is an important ingredient to form the possible C−O−Ti bonds between GQDs and TiO$_2$. Our DFT simulation results strongly support the proposed model for the hybrid formation. The TiO$_2$-GQD hybrid sample exhibited 97% degradation of MB under visible light illumination, which is remarkably high, and the degradation rate constant is 5.2-fold enhanced as compared to that of bare TiO$_2$. The enhanced photodegradation of MB is attributed the rapid interfacial charge transfer from GQDs to TiO$_2$ through the possible C−O−Ti bonds. Free radical scavenger studies reveal that as compared to $O_2^{\circ-}$ radical, the ·OH radical plays a dominant role in the MB degradation. These results provide important clue to the development of hybrid nanocatalysts based on non-metallic GQD and metal oxide semiconductor nanostructures for ensuing optoelectronic, energy and environmental applications.

## Appendix A. Supplementary data

Supplementary data associated with this article can be found, in the online version, at http://dx.doi.org/10.1016/j.apcatb.2017.11.042.

## References

[1] A. Fujishima, K. Honda, Electrochemical photolysis of water at a semiconductor electrode, Nature 238 (1972) 37–38.
[2] G. Hodes, Comparison of dye- and semiconductor-sensitized porous nanocrystalline liquid junction solar cells, J. Phys. Chem. C 112 (2008) 17778–17787.
[3] W. Kim, T. Tachikawa, G.-h. Moon, T. Majima, W. Choi, Molecular-level understanding of the photocatalytic activity difference between anatase and rutile nanoparticles, Angew. Chem. Int. Ed. 53 (2014) 14036–14041.
[4] T. Luttrell, S. Halpegamage, J. Tao, A. Kramer, E. Sutter, M. Batzill, Why is anatase a better photocatalyst than rutile? – Model studies on epitaxial TiO2 films, Sci. Rep. 4 (2014) 4043.
[5] T.A. Kandiel, A. Feldhoff, L. Robben, R. Dillert, D.W. Bahnemann, Tailored titanium dioxide nanomaterials: anatase nanoparticles and brookite nanorods as highly active photocatalysts, Chem. Mater. 22 (2010) 2050–2060.
[6] J. Li, S.K. Cushing, P. Zheng, T. Senty, F. Meng, A.D. Bristow, A. Manivannan, N. Wu, Solar hydrogen generation by a cdS-Au-TiO2 sandwich nanorod array enhanced with Au nanoparticle as electron relay and plasmonic photosensitizer, J. Am. Chem. Soc. 136 (2014) 8438–8449.
[7] X. Yan, Y. Li, M. Li, Y. Jin, F. Du, G. Chen, Y. Wei, Ultrafast lithium storage in TiO2-bronze nanowires/N-doped graphene nanocomposites, J. Mater. Chem. A 3 (2015) 4180–4187.
[8] Y. Yan, W. Shi, Z. Yuan, S. He, D. Li, Q. Meng, H. Ji, C. Chen, W. Ma, J. Zhao, The formation of Ti–H species at interface is lethal to the efficiency of tiO2-based dye-sensitized devices, J. Am. Chem. Soc. 139 (2017) 2083–2089.
[9] J. Zhang, Y. Nosaka, Mechanism of the OH radical generation in photocatalysis with

TiO2 of different crystalline types, J. Phys. Chem. C 118 (2014) 10824–10832.

[10] D. Friedmann, C. Mendive, D. Bahnemann, TiO2 for water treatment: parameters affecting the kinetics and mechanisms of photocatalysis, Appl. Catal. B: Environ. 99 (2010) 398–406.

[11] D. Özer, G. Dursun, A. Özer, Methylene blue adsorption from aqueous solution by dehydrated peanut hull, J. Hazard. Mater. 144 (2007) 171–179.

[12] R.S. Blackburn, Natural polysaccharides and their interactions with dye molecules: applications in effluent treatment, Environ. Sci. Technol. 38 (2004) 4905–4909.

[13] F.-g. Cai, F. Yang, J.-f. Xi, Y.-f. Jia, C.-h. Cheng, Y. Zhao, Ultrasound effect: preparation of PbS/TiO2 heterostructure nanotube arrays through successive ionic layer adsorption and the reaction method, Mater. Lett. 107 (2013) 39–41.

[14] W. Ho, J.C. Yu, Sonochemical synthesis and visible light photocatalytic behavior of CdSe and CdSe/TiO2 nanoparticles, J. Mol. Catal. A: Chem. 247 (2006) 268–274.

[15] Y. Xie, G. Ali, S.H. Yoo, S.O. Cho, Sonication-assisted synthesis of CdS quantum-dot-sensitized TiO2 nanotube arrays with enhanced photoelectrochemical and photocatalytic activity, ACS Appl. Mater. Interfaces 2 (2010) 2910–2914.

[16] Y.-L. Lee, C.-H. Chang, Efficient polysulfide electrolyte for CdS quantum dot-sensitized solar cells, J. Power Sources 185 (2008) 584–588.

[17] K.A. Ritter, J.W. Lyding, The influence of edge structure on the electronic properties of graphene quantum dots and nanoribbons, Nat. Mater. 8 (2009) 235–242.

[18] L.R. Radovic, B. Bockrath, On the chemical nature of graphene edges: origin of stability and potential for magnetism in carbon materials, J. Am. Chem. Soc. 127 (2005) 5917–5927.

[19] G. Rajender, P.K. Giri, Formation mechanism of graphene quantum dots and their edge state conversion probed by photoluminescence and Raman spectroscopy, J. Mater. Chem. C 4 (2016) 10852–10865.

[20] M.A. Montes-Morán, D. Suárez, J.A. Menéndez, E. Fuente, On the nature of basic sites on carbon surfaces: an overview, Carbon 42 (2004) 1219–1225.

[21] S. Wang, I.S. Cole, Q. Li, The toxicity of graphene quantum dots, RSC Adv. 6 (2016) 89867–89878.

[22] P. Roy, P.-C. Chen, A.P. Periasamy, Y.-N. Chen, H.-T. Chang, Photoluminescent carbon nanodots: synthesis, physicochemical properties and analytical applications, Mater. Today 18 (2015) 447–458.

[23] X.M. Li, M.C. Rui, J.Z. Song, Z.H. Shen, H.B. Zeng, Carbon and graphene quantum dots for optoelectronic and energy devices: a review, Adv. Funct. Mater. 25 (2015) 4929–4947.

[24] J. Ali, G.-u.-d. Siddiqui, Y.J. Yang, K.T. Lee, K. Um, K.H. Choi, Direct synthesis of graphene quantum dots from multilayer graphene flakes through grinding assisted co-solvent ultrasonication for all-printed resistive switching arrays, RSC Adv. 6 (2016) 5068–5078.

[25] C.-B. Ma, Z.-T. Zhu, H.-X. Wang, X. Huang, X. Zhang, X. Qi, H.-L. Zhang, Y. Zhu, X. Deng, Y. Peng, Y. Han, H. Zhang, A general solid-state synthesis of chemically-doped fluorescent graphene quantum dots for bioimaging and optoelectronic applications, Nanoscale 7 (2015) 10162–10169.

[26] Y. Zhu, G. Wang, H. Jiang, L. Chen, X. Zhang, One-step ultrasonic synthesis of graphene quantum dots with high quantum yield and their application in sensing alkaline phosphatase, Chem. Commun. 51 (2015) 948–951.

[27] R. Long, Understanding the electronic structures of graphene quantum dot physisorption and chemisorption onto the TiO2 (110) surface: a first-principles calculation, ChemPhysChem 14 (2013) 579–582.

[28] D. Pan, J. Jiao, Z. Li, Y. Guo, C. Feng, Y. Liu, L. Wang, M. Wu, Efficient separation of electron–hole pairs in graphene quantum dots by TiO2 heterojunctions for dye degradation, ACS Sustain. Chem. Eng. 3 (2015) 2405–2413.

[29] K.J. Williams, C.A. Nelson, X. Yan, L.-S. Li, X. Zhu, Hot electron injection from graphene quantum dots to TiO2, ACS Nano 7 (2013) 1388–1394.

[30] L. Lu, Y. Zhu, C. Shi, Y.T. Pei, Large-scale synthesis of defect-selective graphene quantum dots by ultrasonic-assisted liquid-phase exfoliation, Carbon 109 (2016) 373–383.

[31] S. Zhuo, M. Shao, S.-T. Lee, Upconversion and downconversion fluorescent graphene quantum dots: ultrasonic preparation and photocatalysis, ACS Nano 6 (2012) 1059–1064.

[32] P.A. Osorio-Vargas, C. Pulgarin, A. Sienkiewicz, L.R. Pizzio, M.N. Blanco, R.A. Torres-Palma, C. Pétrier, J.A. Rengifo-Herrera, Low-frequency ultrasound induces oxygen vacancies formation and visible light absorption in TiO2 P-25 nanoparticles, Ultrason. Sonochem. 19 (2012) 383–386.

[33] N. Sakai, R. Wang, A. Fujishima, T. Watanabe, K. Hashimoto, Effect of ultrasonic treatment on highly hydrophilic TiO2 surfaces, Langmuir 14 (1998) 5918–5920.

[34] J.C. Colmenares, Sonication-induced pathways in the synthesis of light-active catalysts for photocatalytic oxidation of organic contaminants, ChemSusChem 7 (2014) 1512–1527.

[35] V.G. Pol, R. Reisfeld, A. Gedanken, Sonochemical synthesis and optical properties of europium oxide nanolayer coated on titania, Chem. Mater. 14 (2002) 3920–3924.

[36] M. Xing, F. Shen, B. Qiu, J. Zhang, Highly-dispersed boron-doped graphene nanosheets loaded with TiO2 nanoparticles for enhancing CO2 photoreduction, Sci. Rep. 4 (2014) 6341.

[37] S. Umrao, S. Abraham, F. Theil, S. Pandey, V. Ciobota, P.K. Shukla, C.J. Rupp, S. Chakraborty, R. Ahuja, J. Popp, B. Dietzek, A. Srivastava, A possible mechanism for the emergence of an additional band gap due to a TiOC bond in the TiO2-graphene hybrid system for enhanced photodegradation of methylene blue under visible light, RSC Adv. 4 (2014) 59890–59901.

[38] S. You, M.-W. Chen, D.D. Dlott, K.S. Suslick, Ultrasonic hammer produces hot spots in solids, Nat. Commun. 6 (2015) 6581.

[39] K.S. Suslick, Sonochemistry, Science 247 (1990) 1439–1445.

[40] B.K. Gupta, G. Kedawat, Y. Agrawal, P. Kumar, J. Dwivedi, S.K. Dhawan, A novel strategy to enhance ultraviolet light driven photocatalysis from graphene quantum dots infilled TiO2 nanotube arrays, RSC Adv. 5 (2015) 10623–10631.

[41] A. Qu, H. Xie, X. Xu, Y. Zhang, S. Wen, Y. Cui, High quantum yield graphene quantum dots decorated TiO2 nanotubes for enhancing photocatalytic activity, Appl. Surf. Sci. 375 (2016) 230–241.

[42] P. Sudhagar, I. Herraiz-Cardona, H. Park, T. Song, S.H. Noh, S. Gimenez, I.M. Sero, F. Fabregat-Santiago, J. Bisquert, C. Terashima, U. Paik, Y.S. Kang, A. Fujishima, T.H. Han, Exploring graphene quantum dots/TiO2 interface in photoelectrochemical reactions: solar to fuel conversion, Electrochim. Acta 187 (2016) 249–255.

[43] L.R. Radovic, Active sites in graphene and the mechanism of CO2 formation in carbon oxidation, J. Am. Chem. Soc. 131 (2009) 17166–17175.

[44] L.A. Ponomarenko, F. Schedin, M.I. Katsnelson, R. Yang, E.W. Hill, K.S. Novoselov, A.K. Geim, Chaotic dirac billiard in graphene quantum dots, Science 320 (2008) 356–358.

[45] J. Park, J. Moon, C. Kim, J.H. Kang, E. Lim, J. Park, K.J. Lee, S.-H. Yu, J.-H. Seo, J. Lee, J. Heo, N. Tanaka, S.-P. Cho, J. Pyun, J. Cabana, B.H. Hong, Y.-E. Sung, Graphene quantum dots: structural integrity and oxygen functional groups for high sulfur/sulfide utilization in lithium sulfur batteries, NPG Asia Mater 8 (2016) e272.

[46] Y. Li, Y. Zhao, H. Cheng, Y. Hu, G. Shi, L. Dai, L. Qu, Nitrogen-doped graphene quantum dots with oxygen-rich functional groups, J. Am. Chem. Soc. 134 (2012) 15–18.

[47] G. Rajender, P.K. Giri, Strain induced phase formation, microstructural evolution and bandgap narrowing in strained TiO2 nanocrystals grown by ball milling, J. Alloys Compd. 676 (2016) 591–600.

[48] B. Choudhury, P.K. Giri, Isotype heterostructure of bulk and nanosheets of graphitic carbon nitride for efficient visible light photodegradation of methylene blue, RSC Adv. 6 (2016) 24976–24984.

[49] M.D. Segall, J.D.L. Philip, M.J. Probert, C.J. Pickard, P.J. Hasnip, S.J. Clark, M.C. Payne, First-principles simulation: ideas, illustrations and the CASTEP code, J. Phys.: Condens. Matter 14 (2002) 2717.

[50] J.P. Perdew, K. Burke, M. Ernzerhof, Generalized gradient approximation made simple, Phys. Rev. Lett. 77 (1996) 3865–3868.

[51] J.P. Perdew, W. Yue, Accurate and simple density functional for the electronic exchange energy: generalized gradient approximation, Phys. Rev. B 33 (1986) 8800–8802.

[52] K.N. Kudin, B. Ozbas, H.C. Schniepp, R.K. Prud'homme, I.A. Aksay, R. Car, Raman spectra of graphite oxide and functionalized graphene sheets, Nano Lett. 8 (2008) 36–41.

[53] A.C. Ferrari, D.M. Basko, Raman spectroscopy as a versatile tool for studying the properties of graphene, Nat Nano 8 (2013) 235–246.

[54] W.F. Zhang, Y.L. He, M.S. Zhang, Z. Yin, Q. Chen, Raman scattering study on anatase TiO 2 nanocrystals, J. Phys. D: Appl. Phys. 33 (2000) 912.

[55] T. Ohsaka, F. Izumi, Y. Fujiki, Raman spectrum of anatase, TiO2, J. Raman Spectrosc. 7 (1978) 321–324.

[56] C. Casiraghi, A. Hartschuh, H. Qian, S. Piscanec, C. Georgi, A. Fasoli, K.S. Novoselov, D.M. Basko, A.C. Ferrari, Raman spectroscopy of graphene edges, Nano Lett. 9 (2009) 1433–1441.

[57] D. Bischoff, J. Güttinger, S. Dröscher, T. Ihn, K. Ensslin, C. Stampfer, Raman spectroscopy on etched graphene nanoribbons, J. Appl. Phys. 109 (2011) 073710.

[58] X. Li, X. Wang, L. Zhang, S. Lee, H. Dai, Chemically Derived, Ultrasmooth graphene nanoribbon semiconductors, Science 319 (2008) 1229–1232.

[59] R. Nishinakagawa, K. Matsuda, T. Arai, A. Sawada, T. Terashima, Raman spectroscopy investigations of chemically derived zigzag edge graphene nanoribbons, AIP Adv. 3 (2013) 092111.

[60] A.C. Fernandes, L. Cunha, C. Moura, F. Vaz, P. Carvalho, E. Le Bourhis, P. Goudeau, J.P. Rivière, N.M.G. Parreira, The effect of bombarding conditions on the properties of multifunctional TiCO thin films grown by magnetron sputtering, Surf. Coat. Technol. 202 (2007) 946–951.

[61] T. Skaltsas, X. Ke, C. Bittencourt, N. Tagmatarchis, Ultrasonication induces oxygenated species and defects onto exfoliated graphene, J. Phys. Chem. C 117 (2013) 23272–23278.

[62] S. Zhu, J. Zhang, X. Liu, B. Li, X. Wang, S. Tang, Q. Meng, Y. Li, C. Shi, R. Hu, B. Yang, Graphene quantum dots with controllable surface oxidation, tunable fluorescence and up-conversion emission, RSC Adv. 2 (2012) 2717–2720.

[63] A. Ganguly, S. Sharma, P. Papakonstantinou, J. Hamilton, Probing the thermal deoxygenation of graphene oxide using high-resolution In situ X-ray-based spectroscopies, J. Phys. Chem. C 115 (2011) 17009–17019.

[64] X.-Y. Zhang, H.-P. Li, X.-L. Cui, Y. Lin, Graphene/TiO2 nanocomposites: synthesis, characterization and application in hydrogen evolution from water photocatalytic splitting, J. Mater. Chem. 20 (2010) 2801–2806.

[65] B. Santara, P.K. Giri, K. Imakita, M. Fujii, Evidence of oxygen vacancy induced room temperature ferromagnetism in solvothermally synthesized undoped TiO2 nanoribbons, Nanoscale 5 (2013) 5476–5488.

[66] J. Zhang, Z. Dong, X. Wang, X. Zhao, J. Tu, Q. Su, G. Du, Sulfur nanocrystals anchored graphene composite with highly improved electrochemical performance for lithium–sulfur batteries, J. Power Sources 270 (2014) 1–8.

[67] C.H. Huang, H.L. Bai, Y.L. Huang, S.L. Liu, S.I. Yen, Y.S. Tseng, Synthesis of neutral SiO2/TiO2 hydrosol and its application as antireflective self-cleaning thin film, Int. J. Photoenergy 2012 (2012) 620764.

[68] A. Trapalis, N. Todorova, T. Giannakopoulou, N. Boukos, T. Speliotis, D. Dimotikali, J. Yu, TiO2/graphene composite photocatalysts for NOx removal: a comparison of surfactant-stabilized graphene and reduced graphene oxide, Appl. Catal. B: Environ. 180 (2016) 637–647.

[69] R.K. Biroju, G. Rajender, P.K. Giri, On the origin and tunability of blue and green photoluminescence from chemically derived graphene: hydrogenation and oxygenation studies, Carbon 95 (2015) 228–238.

[70] L.F. Liao, C.F. Lien, D.L. Shieh, M.T. Chen, J.L. Lin, FTIR study of adsorption and

photoassisted oxygen isotopic exchange of carbon monoxide, carbon dioxide, carbonate, and formate on TiO2, J. Phys. Chem. B 106 (2002) 11240–11245.

[71] R. Gone, C. Biswajit, P.K. Giri, In situ decoration of plasmonic Au nanoparticles on graphene quantum dots-graphitic carbon nitride hybrid and evaluation of its visible light photocatalytic performance, Nanotechnology 28 (2017) 395703.

[72] B. Santara, K. Imakita, M. Fujii, P.K. Giri, Mechanism of defect induced ferromagnetism in undoped and Cr doped TiO2 nanorods/nanoribbons, J. Alloys Compd. 661 (2016) 331–344.

[73] S.P. Jovanovic, Z. Syrgiannis, Z.M. Markovic, A. Bonasera, D.P. Kepic, M.D. Budimir, D.D. Milivojevic, V.D. Spasojevic, M.D. Dramicanin, V.B. Pavlovic, B.M.T. Markovie, Modification of structural and luminescence properties of graphene quantum dots by gamma irradiation and their application in a photodynamic therapy, ACS Appl. Mater. Interfaces 7 (2015) 25865–25874.

[74] H. Gao, B. Lu, D. Li, F. Guo, D. Dai, C. Si, G. Liu, X. Zhao, Photoactivity and electronic properties of graphene-like materials and TiO2 composites using first-principles calculations, RSC Adv. 6 (2016) 65315–65321.

[75] X. Pan, M.-Q. Yang, X. Fu, N. Zhang, Y.-J. Xu, Defective TiO2 waes: synthesis, properties and photocatalytic applications, Nanoscale 5 (2013) 3601–3614.

[76] C. Zhou, J. Yan, B. Chen, P. Li, X. Dong, F. Xi, J. Liu, Synthesis and application of ternary photocatalyst with a gradient band structure from two-dimensional nanosheets as precursors, RSC Adv. 6 (2016) 108955–108963.

[77] W. Li, D. Li, Y. Lin, P. Wang, W. Chen, X. Fu, Y. Shao, Evidence for the active species involved in the photodegradation process of methyl orange on TiO2, J. Phys. Chem. C 116 (2012) 3552–3560.